This is a pre-print of the article in Vadose Zone Journal, doi:10.2136/vzj2012.0019, to appear 2013

In Situ Root System Architecture Extraction from Magnetic Resonance Imaging for Application to Water Uptake Modeling

Laura Stingaciu[1], Hannes Schulz[2], Andreas Pohlmeier[1], Sven Behnke[2], Herwig Zilken[3], Mathieu Javaux[1,4], and Harry Vereecken[1]

[1]Forschungszentrum Jülich GmbH, IBG3, Germany
[2]University Bonn, Computer Science VI, Germany
[3]Forschungszentrum Jülich GmbH, JSC, Germany
[4]Université catholique de Louvain, Earth and Life Institute, Louvain-la-Neuve, Belgium

Abstract

An automated method for root system architecture reconstruction from 3D volume datasets obtained from magnetic resonance imaging is developed and validated with a 3D semi-manual reconstruction using virtual reality and a 2D reconstruction using SmartRoot (Lobet et al., 2011). It is tested on the basis of a MRI image of a 25 days old lupin grown in natural sand with a resolution of $0.39 \times 0.39 \times 1.1\,\mathrm{mm}$. The automated reconstruction algorithm was inspired by methods for blood vessel detection in MRI images. It describes the root system by a hierarchical network of nodes which are connected by segments of defined length and thickness, and allows also the calculation of root parameter profiles as root length, surface and apex densities. The obtained root system architecture (RSA) varies in number of branches, segments, and connectivity of the segments, but does not vary in the average diameter of the segments (0.137 cm for semi-manual and 0.143 cm for automatic RSA); total root surface ($127\,\mathrm{cm}^2$ for semi-manual and $124\,\mathrm{cm}^2$ for automatic RSA); total root length 293 cm for semi-manual and 282 cm for automatic RSA), and total root volume ($4.7\,\mathrm{cm}^3$ for semi-manual and $4.7\,\mathrm{cm}^3$ for automatic RSA). The differences in performance of the automated and semi-manual reconstruction is checked by using the root system as input for water uptake modelling with the Doussan model (Doussan et al., 1998). Both systems work well and allow for continuous water flow. Slight differences in the connectivity appear leading to locally different water flow velocities, which are below 30%.

1 Introduction

Root system architecture (RSA) is a crucial plant component of productivity: plant resistance to drought stress, nutrient acquisition and plant yield are strongly influenced by the plant's capacity of developing and adapting its RSA to environmental conditions. Although important progress has been achieved in understanding the molecular and genomic bases of RSA, the interaction of RSA with the soil matrix is far less understood. This is mainly due to the opaque nature of the soil which prevents from direct observation of roots systems and water uptake processes. Novel detailed models which rely on the knowledge of RSA have been developed for simulating nutrient and water uptake or root growth and performing "in situ" experiments for testing and validating the impact of specific root traits (Dunbabin et al., 2002; Doussan et al., 2006; Javaux et al., 2008; Draye et al., 2010). For these not only the RSA is needed but the full network of nodes with their connections. Yet, today, characterizing the 3D RSA in situ is still a challenging task. Various methods were used over the years to obtain root architecture starting with manual drawing (Kutschera, 1960); light transmission (Garrigues et al., 2006); rhizotron mini-cameras (Garre et al., 2011); 3D-imaging platform (Iyer-Pascuzzi et al., 2010; Clark et al., 2011). In the last two decades, however, non-invasive three-dimensional observation techniques with high resolution have been adapted for root soil interaction research. These are X-ray tomography, which probes the physical density of the medium (Wildenschild et al., 2002); neutron tomography (Esser et al., 2010); X-ray microcomputed tomography (Mairhofer et al., 2012); and magnetic resonance imaging MRI (Pohlmeier et al., 2008; Pohlmeier et al., 2010; Rascher et al., 2011). Among the root measurement techniques, MRI possesses several great benefits. MRI can provide 3D images of a strong heterogeneous sample giving the exact location of the various structures within, with high spatial resolution. The knowledge about relaxation properties of root tissue and soil matrix (Pohlmeier et al., 2010; Pohlmeier et al., 2012a) can be used to differentiate between roots and soil and obtain high resolution 3D architecture of roots growing in natural soil. As compared to 2D scans or pictures, 3D imaging may also bring more precise informations on branching connection, explored soil volume and branching angles. Ideally, all the connections between root segments should be characterized in a unique way (which is not the case with a 2D image). Limitations in using high field MRI for root-soil imaging are mainly due to the presence of air bubbles and para- or ferromagnetic particles in natural soil which lead to susceptibility artifacts caused by local magnetic field inhomogeneities. This shifts the resonance frequency of the root tissue which is translated by the subsequent image reconstruction in a shifted location. The roots appear "pitted" or even gaps in the root strand occur (Menzel et al., 2007). Another difficulty for achieving good contrast is in wet soils near saturation where transverse relaxation times of the soil matrix are relatively long compared to the relaxation in the root issue. Here, long echo times must be used for fading out signal from soil. It should be noted that also the other 3D imaging techniques mentioned above have in common with MRI that information about the course of the root strands is sometimes interrupted and noisy. Therefore such data can not be utilized as input for e.g. inverse modelling or analyis of the root system architecture.

What is needed is an image processing procedure, which finally yields a 3D network of root nodes that represents the RSA with no gaps, since such gaps prevent water flow. In addition, such a reconstruction should allow for characterization of the root diameter and exact location distributions.

In this paper, we introduce a novel automated method to recognize and reconstruct the 3D-RSA using high resolution (0.39 mm) MRI dataset of a three week-old lupin plant grown in sandy soil material (Pohlmeier et al., 2012b). For validation this automated method is compared with a semi-manual 3D reconstruction procedure in virtual reality and a 2D analysis. The automatic reconstruction was performed using software developed in Bonn University based on a tube similarity measure for blood vessel detection in MRI images (Sato et al., 1998; Frangi et al., 1998). The semi-manual reconstruction is performed using the virtual reality system Pi-casso (JSC, FZ Jülich) developed by S. Wienke and H. Zilken (Winke, 2010) based on *ViSTA* software platform (Virtual Reality for Scientific Technical Application) developed at RWTH Aachen (Assenmacher and Kuhlen, 2010). The 2D skeletonisation is based on SmartRoot algorithm developed by Lobet et al. (2011). The comparison between the different methods is based on statistical differences between topological indices. A transient water flow experiment using the Doussan et al. (1998) model was simulated using both 3D root structures (semi-manual and automatic) to assess the influence of the observed differences between the root structures on water potential and water flux within the root xylem.

2 Methods

Our experiment consisted in monitoring the water content distribution dynamics in a pot with a lupin during a drought experiment. A lupin seedling was planted in a 8×10 cm Perspex cylinder, filled with medium sand as growing medium, and watered from the bottom with Hoagland nutrition solution. Nine days after germination, the cylinder was saturated to a water content of $0.33\,\mathrm{cm}^3\mathrm{cm}^{-3}$ and sealed at bottom and top so that water loss was possible only by transpiration. During the following period, MRI images of the root system were taken after 0, 11, and 16 days to monitor root system development during increasing drought stress. From these series, the image obtained at the last date is chosen here for further analysis, since in this state it was most similar to the photographs taken after finishing the experiments. The MRI experiments were performed on a 4.7 T vertical bore superconducting magnet (Magnex Scientific, UK) operated by a Varian console. The NMR RF-resonator is a birdcage-type resonator with an internal diameter of 100 mm. The signal from the soil was efficiently suppressed by a long echo time of 20 ms and further by applying a threshold of 16 percent of the maximum signal. Repetiton time was 30s. The field of view was 100×100 mm at a matrix size of 256x256 pixles resulting in a resolution of 0.39 mm in-slice and a slice thickness of 1.1 mm, and 120 slices were monitored in interleaved mode. The total measuring time was about 4 hours for two acquisitions Pohlmeier et al. (2012b).

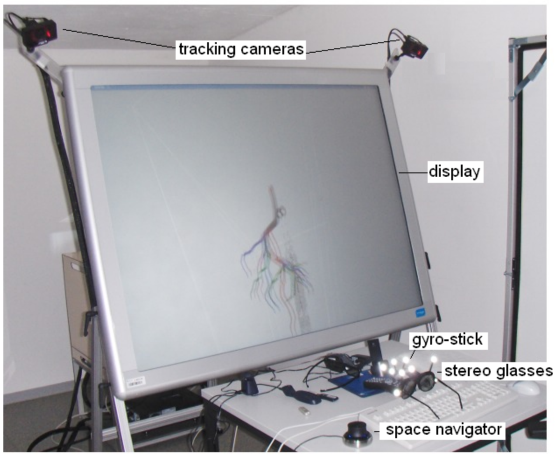

Figure 1: Pi-Casso work station used in the semi-manual reconstruction of the lupin RSA. Two projections of the 3D image with orthogonal polarization are overlaid on the display and can be viewed by the stereo glasses. The tracking cameras monitor the motion of the users head, the 3D image can be moved and rotated by the space navigator, and nodes are defined by clicking using the gyro-stick (a 3D mouse).

2.1 Automatic Reconstruction

In this section, we summarize the algorithm for automatic root reconstruction described by Schulz et al. (2012). The algorithm starts with a 3-dimensional MRI image. The unit of a 3D image is a *voxel*[1]. Each voxel is described by a single grey value representing the signal intensity.

We first enhance the raw data by emphasizing tubular structures (the roots) using an algorithm developed by Frangi et al. (1998) for blood vessel detection in medical MRI images. This results in another 3D image, where values in voxels are larger if the local structure of voxels has similarity to a tube.

The root model we desire should, however, be defined in terms of root segments and branches, not in terms of voxels. Our multi-step procedure for the automatic extraction of the root model from the 3D image is summarized hereafter.

2.1.1 Finding Tubular Structures

Tubular structures (root segments, in our case) can be found in the second order derivatives of an image (Frangi et al., 1998). Locally, the image structure is similar to a tube if in one direction (where the root grows), grey value does not change much, while in the other two directions (orthogonal to the first one), grey value drops off equally fast and

---

[1] cf. pixel in 2D images

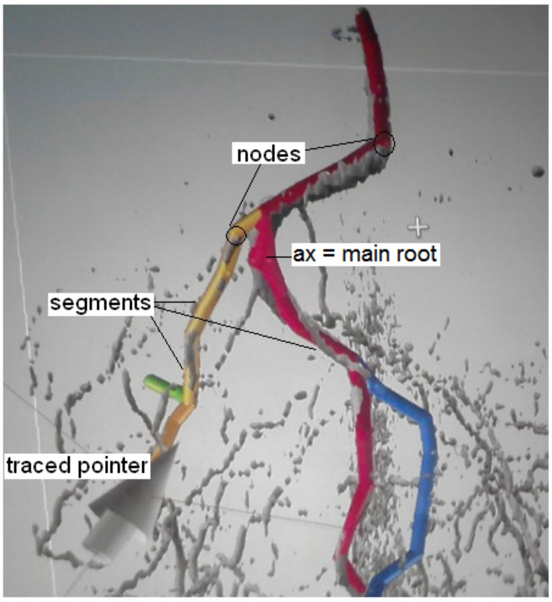

Figure 2: Construction of nodes and segments using the traced pointer on Pi-Casso station. A different color is automatically selected by the system for each new branch. Also shown is the 3D traced pointer, which is a 3D equivalent of the well known 2D pointer on computer monitors

rapidly. Here, the change in grey value is captured by the eigenvalues of the Hessian matrix, while directions are captured by the eigenvectors.

Whether a tube is found depends on the scale. Small roots are found when the Hessian is calculated in small neighborhood, large roots are found when larger window is considered. The neighborhood can be varied more efficiently by convolving the image with a Gaussian distribution with standard deviation σ first and then using a fixed neighborhood (e.g. all adjacent voxels) to determine the Hessian. The parameter σ is chosen proportional to the size of the roots we intend to find.

We first pre-process the MRI image by up-sampling to isotropic (equal edge lengths) voxels using cubic spline interpolation. The resulting image is then convolved with a Gaussian distribution at scale σ and the tube similarity measure by Frangi et al. (1998), a function of the eigenvalues, is computed. We repeat this process for all scales and find the maximum value for each voxel.

In the resulting 3D image, each voxel is represented by a number which is larger if there exists a scale at which the neighborhood of the voxel has the appearance of a tube.

2.1.2 Determining the Root collar Position

The starting point for model extraction will be the root collar, i.e., the position in the 3D image where the plant exits the ground. We know the approximate slice (z coordinate) in the 3D image where this happens due to the measuring process. To find the other coordinates robustly, we convolve the slice with a Gaussian with large σ to remove maxima which are due to measurement noise. The maximum in the smoothed slice then has the x and y coordinates of the root collar.

2.1.3 Determining the Connection between Root Elements

All parts of the root must be connected somehow to the collar position determined above. This intuition is captured by the concept of a *tree* in the graph-theoretical sense. To ease discussion in the following, we briefly introduce several technical terms. A *directed graph* is a set of *nodes* and a set of tuples containing two nodes each. One tuple—usually referred to as child and parent—defines a *directed edge.* A *tree* is a directed graph where every node has exactly one parent. One node is exempt from this rule, it has no parents. This is the so-called *root node*, which in our case corresponds to the root collar.

For every voxel, many paths may lead to the root collar, but we need to choose one. We decided to select the path where most way-points are similar to a tube. For this purpose, we define a cost function between two adjacent[2] voxels $\mathbf{x}_s$ and $\mathbf{x}_t$ as

$$w(\mathbf{x}_s, \mathbf{x}_t) = \|\mathbf{x}_t - \mathbf{x}_s\| \exp\left(-\omega(\mathcal{V}_s + \mathcal{V}_t)\right), \qquad [1]$$

where $\mathcal{V}_s$ is the tube similarity measure at position $\mathbf{x}_s$ and ω is a constant, which we set to 10. For each voxel in the 3D image we find the path for which the cost is minimal. We implement this search efficiently using the Dijkstra algorithm (Dijkstra, 1959), which

---

[2] We use a 26-neighborhood. In 3D, a voxel has 6 direct and 20 diagonally connected neighbors.

finds shortest paths for all voxels simultaneously. For each voxel we then know (a) the distance in terms of costs to the root collar and (b) a predecessor, that is, the voxel in its neighborhood which decreases the cost towards the root collar the most. This defines *tree* as introduced above.

2.1.4 Model Construction

Every voxel is now connected to the root collar position, but we already know that not all voxels are part of the root structure. The voxel-based tree needs to be pruned by removing branches which only represent part of the soil, leaving the tree representing the root system.

For this purpose, we carefully select voxels which are definitely part of the root system. They, and the whole path connecting them to the root collar are then retained for the final root system tree.

The selection is based on two thresholds. The grey value of a selected voxel must be above some first threshold νN, where N is the average noise level of the imaging procedure estimated in air above ground. If the signal-to-noise ratio is low and ν is small, this is not sufficient, as all spurious measurements would be part of the root system tree. We therefore define a second threshold, accepting only voxels for which the mass of their subtree (i.e. all their children, grandchildren, $\dots$) is larger than a threshold μN. The two thresholds can be chosen manually or automatically if the true root system is known—see Schulz et al. (2012) for details.

The retained graph can now be represented as a graph data structure instead of an image. The retained voxels are the nodes of this graph, while the predecessor relationship defines its directed edges.

2.1.5 Subvoxel Positioning

To determine the lengths, surface and volume of root, high-precision positioning of nodes is essential. So far, nodes are positioned at voxel centers, where we initialized them. Voxel centers are merely an artefact of the MRI procedure, the true root likely does not pass through voxel centers. We now apply a iterated mean-shift procedure to move the nodes to the center of the root with subvoxel precision. At each node n at position $\mathbf{x}_n$, we estimate a covariance matrix C_n in a radius of 3 mm and determine its eigenvalues $\lambda_1 \leq \lambda_2, \leq \lambda_3$ as well as corresponding eigenvectors $\mathbf{v}_1, \mathbf{v}_2, \mathbf{v}_3$. If $\lambda_3 > 1.5\lambda_2$, we can assume that a clear direction is defined and $\mathbf{v}_3$ corresponds to the local root direction. We then move the node to the mean of a neighborhood in the voxel grid, weighted by the tube similarity measure $\mathcal{V}$. To do so, we choose a 4-neighborhood of $\mathbf{x}_n$ in the plane spanned by $\mathbf{v}_1$ and $\mathbf{v}_2$, and evaluate $\mathcal{V}$ by linear interpolation.

Nodes where no main principal axis can be determined ($\lambda_3 < 1.5\lambda_2$) are moved to the mean of their immediate neighbors in the root graph. We iterate these steps until positions stop changing significantly.

2.1.6 Radius Estimation

We determine the radius of a root assuming a (truncated) symmetric Gaussian cross-section profile of roots. First, we fit a radial Gaussian function $M_n(\mathbf{r}) = a\exp(-b\|\mathbf{r}\|^2) + \nu N$ to the MRI data in the plane defined by the second and third eigenvector of the covariance matrix C_n at every node n. The parameters a and b are estimated using unconstrained least squares optimization with the Levenberg-Marquardt algorithm starting at $a = L(\mathbf{x}_n)$, the interpolated MRI voxel intensity at the position of node n, and 1/5 of the expected maximum root radius $\mathbf{r}_{max}$ for the width, i. e. $b = 12.5/\mathbf{r}^2_{max}$. Starting with a thin root hypothesis biases the local optimization towards thin roots and avoids merging information of two neighboring root segments. The radius is set to b. Since estimates are noisy, especially for thin roots, we smooth the radius using a robust median filter over the closest six nodes in the graph.

2.1.7 Algorithm Runtime

Many parts in the described algorithm are inherently parallel. We therefore use a $12 \times 2.67\,\mathrm{GHz}$ core Intel machine. The runtimes reported are for the $256 \times 256 \times 120$ reference root, which is upsampled to $256 \times 256 \times 256$. Most processing time is spent for calculation of the tube similarity measure (30 s per scale). The shortest path selection amounts to 3 min. Sub-voxel positioning takes 15 s, radius estimation 1.5 min. All other steps have runtimes totaling in less than 1 min. The complete dataset can therefore be processed in about 10 min. This is significantly shorter than the measuring time for one MRI image of the whole root system which takes about 1 hour.

2.2 Manual reconstruction using virtual reality (VR)

The automatically reconstructed RSA is compared with a semi-manual method using a 3D virtual reality system. The setup of the virtual reality system is shown in Fig. 1. It contains a virtual reality engine and input/output hardware to supply the platform for simulation. The engine reads the input devices, accesses databases, performs updates for real-time calculation of the virtual world and is responsible for presenting the results to the output device. These tasks are performed by a desktop computer in cooperation with the visualization system PI-casso which includes a display, tracking cameras, tracked stereo glasses, tracked gyro-stick (a 3D mouse) and the space navigator as output/input devices. *ViSTA* is a software platform that allows for integration of VR technology and interactive 3-D visualization (Assenmacher and Kuhlen, 2010). After cutting off voxels below a manually determined threshold, the MRI root image is visualized in VR. The reconstruction of the root was carried out manually by creating nodes and root segments using the gyro-stick, which is represented on the 3D working environment by a traced pointer (Fig. 2). The user first defines the parent node, which is the point, where the shoot enters the soil domain. This is termed in Sec. 2.1.2 as “root of the tree” in the graph theoretical sense. Then further descendants nodes are defined and automatically connected to the parent node by segments. The user must also define the thickness of the segments, which later defines their surface area through which water uptake takes place, by the gyro-stick. Then further nodes and segments are added until the whole root system is defined. The developed software provides the user with the option to store and later reload the reconstructed root system. The final root system architecture is hierarchically structured in a single tree and stored in ASCII format in the corresponding RSWMS input file (Javaux et al., 2008). In addition to the x, y, and z coordinates of each node, the *ID-s* number of the node and the branching order, the surface area of each root segment, the length of the root segment and its mass are also calculated. The surface area of each segment is a morphological characteristic of particularly importance because it affects the amount of water absorption. The time needed for the whole procedure was about 3 hours. Detailed information about development of the virtual reality system can be found in Winke (2010).

2.3 2D skeletonisation

The 2D skeletonization of the lupin root is based on SmartRoot image analysis toolbox developed by Lobet et al. (2011). Firstly, the root was extracted from the soil, washed and spread on a horizontal plate to avoid as much as possible overlapping of branches. Next, the root was photographed. The 2D photo was used to trace the root architecture and topology using SmartRoot. Citing the authors, “SmartRoot is semiautomated image analysis software that combines vectorial representation of root objects with a tracing algorithm that determines the center of the root at a picked position by mouse click and, continues with a stepwise reconstruction of the root segments backward and forward to the tip and the basis of the root. It is implemented as a plug-in of the ImageJ software (Rasband, 2011)”. Detailed explanations on how SmartRoot works can be found in Lobet et al. (2011).

2.4 Simulation of root water uptake

As stated before, one of the main aims of this paper is to establish an automated reconstruction method that reliably creates a continuous, hierarchical root system from 3D volume graphics data sets. Therefore as final check of the convenience of the obtained root system, we have simulated root water uptake by the Doussan et al. (1998) model. It aims in finding the pressure head and root water uptake distribution in the root given certain collar boundary conditions and soil pressure head distribution. In the Doussan model, the pressure head in the roots is obtained by solving a system of equations:

$$\mathbf{C} * \mathbf{\Psi} = \mathbf{Q}, \qquad [2]$$

where $\mathbf{C}$ is the conductance matrix, $\mathbf{Q}$ contains the soil physical parameters (water content, hydraulic conductivity), and $\mathbf{\Psi}$ is the root (xylem) water potential. A complete description of this equation is given in Doussan et al. (1998). The boundary conditions were defined at the root collar as a water flux of $1\,\mathrm{cm\,day^{-1}}$. The model was initialized in pressure head ($-100\,\mathrm{cm}$) and constant axial and radial conductivities of the roots were assumed for the entire root network. The conductivity values used in the simulations were obtained from literature to be $1.67 \cdot 10^{-9}\,\mathrm{cm\,s^{-1}cm^{-1}}$ (recalculated from $1.7 \cdot 10^{-7}\,\mathrm{m\,MPa^{-1}s^{-1}}$, (Bramley et al., 2007)) for the radial conductivity, the highest value they found for lupin, and $2.45 \cdot 10^{-7}\,\mathrm{cm}^4\mathrm{s}^{-1}\mathrm{cm}^{-1}$ for the axial conductivity from the same source.

3 Results and Discussions

The obtained MRI image of the lupin root is presented in Fig. 3a. Discontinuities along root branches can easily be observed (see also Fig. 2). These large gaps are not realistic, they are the result of high threshold values imposed to differentiate the root structure from the surrounding soil. This effect demonstrates that reconstruction of the root system architecture (RSA) is needed to obtain a continuous structure which is necessary for simulation and evaluation of hydraulic events. The manually reconstructed root architecture as obtained from the Pi-casso virtual system is presented in Fig. 3b. The reconstruction allows root system skeletonisation, e. g. transformation of MRI image into a compatible file, which contains spatial coordinates of nodes, branch order and information about segments dimension necessary for simulating root water uptake. The root skeleton obtained from Pi-casso semi-manual reconstruction has 1 ax (main root), 105 branches, 106 tips, and 3308 segments. In comparison, the root architecture obtained by automatic reconstruction is presented in Fig. 3c. The root skeleton obtained by automatic reconstruction has 1 ax (main root), 226 branches, 227 tips, and 2667 segments. When visually compared with *"semi-manual"*, the *"automatic"* RSA show small differences in the connectivity of the branches due to the fact that the automatic reconstruction is based on Dijkstra algorithm, which searches for the minimum-cost path to connect two neighboring nodes, which is not necessarily optimal according to a biological model. In order to quantify the differences between the two reconstructions, various indices were estimated based on the reconstructed RSA and summarized in Tab. 1. It can be seen that the obtained RSA vary in number of branches, segments, and connectivity of the segments, but do not vary extensively in the average diameter of the segments (0.137 cm for *semi-manual* and 0.143 cm for *automatic* RSA); total root surface (127 cm^2 for *semi-manual* and 124 cm^2 for *automatic* RSA); total root length 293 cm for *semi-manual* and 282 cm for *automatic* RSA), and total root volume (4.7 cm^3 for *semi-manual* and 4.7 cm^3 for *automatic* RSA). In general, both RSA exhibit comparable values for these parameters.

These parameters are compared for a better assessment with parameters obtained by tracing the same root from a 2D photo using SmartRoot image analysis toolbox developed by Lobet et al. (2011). The 2D photo together with its tracing is shown in Fig. 3d. It shows overlapped branches which cannot trivially be traced individually, as well as thin roots close to higher order branches that have been considered as one thicker or thinner segment when root diameter was estimated. The calculated parameters from the 2D skeletonization are also included in Tab. 1. The total root lengths obtained by all three methods agree quite satisfactory. This proves that MRI has detected the majority of all roots. The major difference is smaller average segment diameter obtained from 2D (0.078 cm) compared to the reconstructed data (0.137 and 0.143 cm, respectively). This results in smaller root surface areas and smaller total root volumes. The reasons for this effect are not yet fully clear. One possible explanation is the partial volume effect of MRI data, which classifies all voxels as roots irrespective of whether they are filled

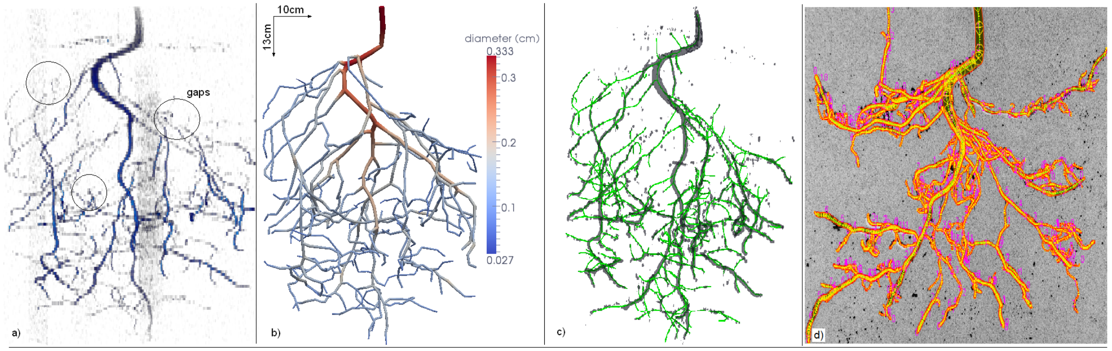

Figure 3: 25 days old root system of lupin grown in sandy soil: a) original MRI image (from (Pohlmeier et al., 2012b)) after subtraction of a threshold of 16 percent with respect to highest voxel intensity. Encircled are three exemplary gaps in the root strands, b) hand-labeled reconstruction using the virtual reality system, c) automatic reconstruction superimposed on isometric rendering of thresholded raw data, d) 2D photo of the spread root and its SmartRoot tracing. Yellow marks represent the midline of the branches and the estimated segment diameters. Note that all images have a field of view of 10.0 × 13.2 cm.

completely or only partially by a root.

Further, we quantify for the observed variations with the depth of the soil domain by describing the root architecture as density functions of both, geometrical and topological properties (Fig. 4) according to the mathematical approach of Dupuy et al. (2010). The soil domain is discretized and the density profiles of various root system parameters are calculated from the spatial location of the root segments and tips as functions of grid element volume. The root length density is the total segment length divided by the grid volume and integrated over the axial slice. Analogously, the root surface and root volume densities are defined as integral segment and volume per slice. Root branch and apex densities aim in finding the distribution of the nodes at which branching occurs and the distribution of the apexes over the slice volume. The root length density, root surface density and root volume density are nearly identical in values and shape of the profiles. Also, the shapes agree very well with the root density profile obtained directly from the evaluation of the MRI images by axial integration (Pohlmeier et al., 2012b).

The distribution of the number of roots per depth of the soil differs slightly between the two structures with less roots for automatic RSA, especially in the upper part of the soil domain. This could be explained by different threshold values imposed in both, semi-manual and automatic reconstruction to suppress the signal from soil. Due to differences in the data processing (single threshold for semi-manual RSA and two thresholds for automated RSA, see Sec. 2.1.4) these threshold values can't be set equal. Therefore, sparse pixels defining very fine roots with signal intensity close to the threshold value may faint out together with soil signal. The shape of the apex densities is similar for both root structures with the difference that for automatic RSA the profiles are shifted to higher values. This can be explained by the differences in the number of traced root segments. The automated reconstruction generates more root branches and thus root apices, by artificially cutting root segments which should be connected. However,this is not a defining parameter of the roots since in both methods the number of segments can be easily influenced and modified by the user. Branching density profiles show that for the automatic RSA the branching occurs in a more shallow soil layer than for semi-manual RSA. This can be a measure of the differences in the connectivity of the branches which varies for the automatic reconstruction due to the limitations of Dijkstra algorithm.

In order to assess how these differences in the root architecture affect the root water uptake, simulations using both root structures were performed using the algorithm developed by Doussan et al. (1998). The results of the simulation are shown in Fig. 5. The water potential and radial flux of the semi-manual automatic RSA are displayed, with visible differences both in values as well as in their distribution along the root network. The evolution of the water potential and water flux follows closely the transpiration rate applied at the root collar, but the response decreases in the direction of the root base, for both structures as a result of uniformity assumed in the hydraulic conductivity distribution. The differences in the distribution of water potential and radial flux are a clear indication of the differences between roots structure since the most visible differences are localized in areas with differences in the connectivity of the branches. The most obvious difference occur in the central, top region. In the semi-manual RSA the local fluxes are distributed over more root segments than in the automatic RSA. Hence, in

Nr.	Parameter	Units	Manual	Automatic	SmartRoot
1	Nr. of axes	-	1	1	1
2	Nr. of branches	-	105	226	187
3	Nr. of segments	-	3308	2667	1799
4	Avg. diameter of the segments	cm	0.137	0.143	0.078
5	Standard deviation of avg. diameter	-	0.056	0.05	0.03
6	Minimum diameter	cm	0.026	0.055	0.025
7	Maximum diameter	cm	0.332	0.408	0.331
8	Total root length	cm	293.5	281.7	281.7
9	Total root surface	cm^2	127.3	123.9	90.93
10	Total root volume	cm^3	4.765	4.705	3.78
11	Average root collar flow	$\mathrm{cm\,day}^{-1}$	0.007	0.008	–

Table 1: Roots calculated parameters. Note that the average transpiration value was calculated for an imposed potential transpiration of $1\,\mathrm{cm\,day}^{-1}$

this region the local flow velocities are with about 0.7 $\mathrm{cm\,day}^{-1}$ somewhat smaller than in the automatic RSA (about $1.2\,\mathrm{cm\,day}^{-1}$).

4 Summary and Conclusions

In the present study, we tested two methods of reconstructing the 3D root system architecture of a lupin plant, grown in sandy soil, from high-resolution MRI images, with respect to root system connectivity, water uptake and transport properties. The first method was semi-manual reconstruction using virtual reality and the second method was an automatic reconstruction based on local detection of tubular structures and globally enforced connectivity. The methods were validated by a 2D classical skeletonization. The obtained root structures showed variations in the connectivity of segments. Less differences were encountered in the root parameters (number of branches and segments, diameters of the segments, total surface, and total volume). This is assumed to be influenced by different threshold values imposed in semi-manual and automatic reconstruction of the roots to differentiate the root structure from the soil domain. From the outcome of the two reconstructions, it was shown that automatic annotation gives objective results of equal quality to the semi-manual one, suitable for large-scale experiments and repeatable for the same type of soil and root. Qualitatively, both methods shift root diameter towards larger values in comparison with the MRI image resolution. To assess the influence of the observed differences between the root structures on root water uptake and xylem pressure head distribution, simulations using Doussan numerical model were performed in a homogeneous soil and assuming a homogeneous distribution of root hydraulic conductivity. From the outcome of the simulations, it was shown that the distribution of the water flux and xylem water potential is slightly different for each root structure, with lower values for the automatic reconstruction. The main differences in water flux and xylem water potential are localized in areas where the two root structures show differences in segments connectivity. This is expected, since in the automatic annotation algorithm no experimental information about root segments connectivity is introduced. Incorporating such knowledge is subject of further research.

Acknowledgments

The authors are grateful to Sandra Wienke (RWTH-Aachen) for developing Picasso virtual system software during her master thesis; The CROP.SENSe.net research network (Project B4) for financial support; Dagmar van Dusschoten and Horst Hardelauf (FZ-Juelich, IBG2/IBG3) for technical support; Guillaume Lobet (UCL, Belgium) for SmartRoot code; Natalie Schroeder and Jan Vanderborght (FZ-Juelich) for helpful discussions.

References

Assenmacher, I. and T. Kuhlen (2010). *The ViSTA Virtual Reality Toolkit.* URL: `http://www.rz.rwth-aachen.de/aw/cms/rz/Themen/Virtuelle_Realitaet/research/~piz/vr_software_vista/`.

Bramley, H. et al. (2007). „Comparison between gradient-dependent hydraulic conductivities of roots using the root pressure probe: the role of pressure propagations and implications for the relative roles of parallel radial pathways“. In: *Plant, Cell and Environment* 30, pp. 861–874.

Clark, R. T. et al. (2011). „Three-dimensional root phenotyping with a novel imaging and software platform“. In: *Plant Physiology* 156, pp. 455–465.

Dijkstra, E. W. (1959). „A note on two problems in connexion with graphs“. In: *Numerische Mathematik* 1, pp. 269–271.

Doussan, C. et al. (1998). „Modelling of the hydraulic architecture of root systems: an integrated approach to water absorption – model description“. In: *Annals of Botany* 81, pp. 213–223.

Doussan, C. et al. (2006). „Water uptake by plant roots: II – Modelling of water transfer in the soil root-system with explicit account of flow within the root system – Comparison with experiments“. In: *Plant and Soil* 283, pp. 99–117.

Draye, X. et al. (2010). „Model-assisted integration of physiological and environmental constraints affecting the dynamic and spatial patterns of root water uptake from soils“. In: *J. Exp. Bot.* 61, pp. 2145–2155.

Dunbabin, V. et al. (2002). „Modelling the interactions between water and nutrient uptake and root growth“. In: *Plant and Soil* 239, pp. 19–38.

Dupuy, L. et al. (2010). „The dynamics of root meristem distribution in the soil“. In: *Plant, Cell and Enviroment* 33, pp. 358–369.

Esser, H. G. et al. (2010). „Neutron radiography and tomography of water distribution in the root zone“. In: *J. Plant Nutr. Soil Sci.* 173, pp. 757–764.

Frangi, A. F. et al. (1998). „Multiscale vessel enhancement filtering“. In: *Medical Image Computing and Computer-Assisted Interventation (MICCAI)*, pp. 130–137.

Garre, S. et al. (2011). „Parameterizing a dynamic architectural model of the root system of spring barley from minirhizotron data“. In: *Vadose Zone J.* submitted.

Garrigues, E. et al. (2006). „Water uptake by plant roots: I – Formation and propagation of a water extraction front in mature root systems as evidenced by 2D light transmission imaging“. In: *Plant and Soil* 283, pp. 83–98.

Iyer-Pascuzzi, A. S. et al. (2010). „Imaging and analysis platform for automatic phenotyping and trait ranking of plant root systems“. In: *Plant Physiology* 152, pp. 1148–1157.

Javaux, M. et al. (2008). „Use of a three-dimensional detailed modeling approach for predicting root water uptake“. In: *Vadose Zone J.* 7, pp. 1079–1088.

Kutschera, L. (1960). *Wurzelatlas mitteleuropäischer Ackerunkräuter und Kulturpflanzen.* DLG, Frankfurt am Main.

Lobet, G. et al. (2011). „A novel image analysis toolbox enabling quantitative analysis of root system architecture“. In: *Plant Physiology* 157, pp. 29–39.

Mairhofer, S. et al. (2012). „RooTrak: automated recovery of three-dimensional plant root architecture in soil from X-Ray microcomputed tomography images using visual tracking“. In: *Plant Physiology* 158, pp. 561–569.

Menzel, M.I. et al. (2007). „1H-NMR imaging and relaxation mapping - a tool to distinguish the geographical origin of German white asparagus?“ In: *Journal of Plant Nutrition and Soil Science* 170, pp. 1–14.

Pohlmeier, A. et al. (2008). „Changes in Soil Water Content Resulting from Ricinus Root Uptake Monitored by Magnetic Resonance Imaging“. In: *Vadose Zone Journal* 7, pp. 1010–1017.

Pohlmeier, A. et al. (2010). „MRI in Soils: Determination of Water Content Changes Due to Root Water Uptake by Means of a Multi-Slice-Multi-Echo Sequence (MSME)“. In: *The Open Magnetic Resonance Journal* 3, pp. 69–74.

Pohlmeier, A et al. (2012a). „Nuclear Magnetic Resonance Imaging (MRI) Techniques for Visualization of Root Soil Processes“. In: *Tomography and Imaging of Soil-Water-Root.* Ed. by S. H. Anderson and J. W. Hopmans. in print.

Pohlmeier, A. et al. (2012b). „Root system growth and water uptake of lupin in natural sand: 3D visualization by MRI“. In: *Magnetic Resonance Imaging* submitted.

Rasband, V.S. (2011). *ImageJ.* URL: `http://imagej.nih.gov/ij/`.

Rascher, U. et al. (2011). „Non-invasive approaches for phenotyping of enhanced performance traits in bean“. In: *Functional Plant Biology* 38, pp. 968–983.

Sato, Y. et al. (1998). „Three-dimensional multi-scale line filter for segmentation and visualization of curvilinear structures in medical images“. In: *Medical Image Analysis* 2, pp. 143–168.

Schulz, H. et al. (2012). „3D reconstruction of plant roots from MRI images“. In: *International Conference on Computer Vision Theory and Applications (VISAPP).*

Wildenschild, D. et al. (2002). „Using X-ray computed tomography in hydrology: systems, resolutions, and limitations“. In: *Journal of Hydrology* 267, pp. 285–297.

Winke, S. (2010). „Entwicklung einer software zur bestimmung morphologischer informationen von wurzelsystemen mit Virtual Reality techniken“. MA thesis. Aachen University of Applied Sciences.

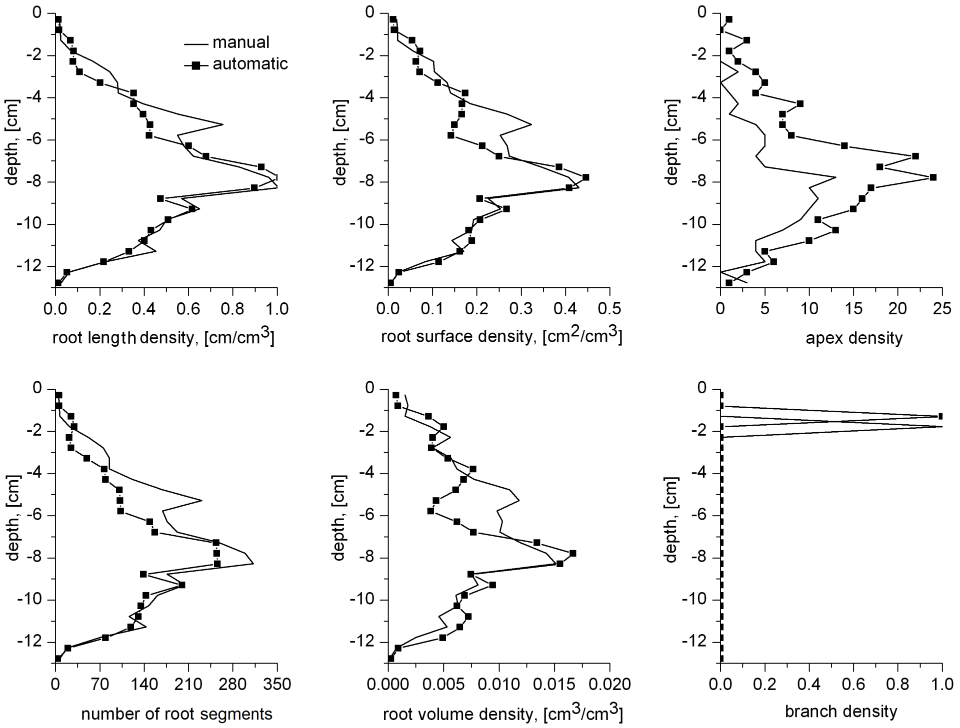

Figure 4: Vertical profiles of root parameters obtained from semi-manual (—) and automated (-•-) reconstruction using the 3D MRI image of the 25 days old lupin root system

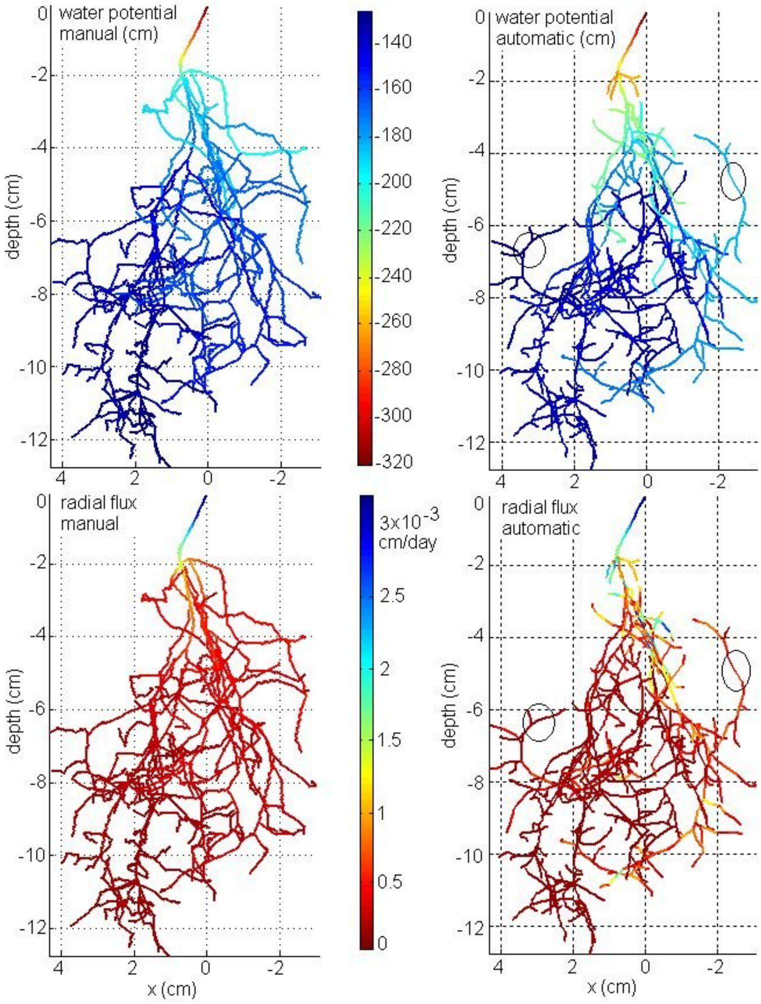

Figure 5: Results of water flux simulation in the root system with the Doussan model using the semi-manual (left column) and automated RSA (right column). Top row: Water potential and bottom row: water flux distribution. The circles mark region of different connectivity assumed by the automatic method (upward growing roots).